ADVANCED MATERIALS

Self-Structural Healing of Encapsulated Perovskite Microcrystals for Improved Optical and Thermal Stability

Ruxue Li, Bobo Li, Xuan Fang, Dengkui Wang, Yueqing Shi, Xiu Liu, Rui Chen,* and Zhipeng Wei*

Perovskite materials and their optoelectronic devices have attracted intensive attentions in recent years. However, it is difficult to further improve the performance of perovskite devices due to the poor stability and the intrinsic deep level trap states (DLTS), which are caused by surface dangling bonds and grain boundaries. Herein, the $CH_3NH_3PbBr_3$ perovskite microcrystal is encapsulated by a dense Al_2O_3 layer to form a microenvironment. Through optical measurement, it is found that the structure of perovskite can be healed by itself even under high temperature and long-time laser illumination. The DLTS density decreases nearly an order of magnitude, which results in 4–14 times enhancement of light emission. The observation is ascribed to the micron-level environment, which serves as a self-sufficient high-vacuum growth chamber, where the components of the perovskite are completely retained when sublimated and the decomposed atoms can re-arrange after thermal treatment. The modified structure showing high thermal stability is able to maintain excellent optical and lasing stability up to 2 years. This discovery provides a new idea and perspective for improving the stability of perovskite and can be of practical interest for perovskite device application.

1. Introduction

Due to the long charge diffusion length (175 µm),[1] high carrier mobility (164 cm^2 V^{-1} s^{-1}),[1] high optical absorption coefficient (10^4–10^5 cm^3),[2] high gain coefficient (1000 cm^{-1}),[3,4] and tunable direct band gaps,[5,6] perovskite materials have been recognized as one of the most promising semiconductors for optoelectronics. Within a very short period of time, the power conversion efficiency of perovskite solar cells have already exceeded 25%.[7,8] In addition, multicolor light-emitting diodes (LEDs) and low threshold lasers have also been realized.[3,4,9–11] Although excellent perovskite optoelectronic devices can be achieved by further optimizing the material and device architectures,[12–14] the poor stability of the materials has seriously affected their commercial applications. For example, the lasing threshold of a perovskite laser can be as low as 10 µJ cm^{-2}, but the service life is only tens of minutes. For perovskite LEDs, external quantum efficiency higher than 20% has been achieved. However, the operating temperature is between 60 and 100 °C, which is extremely unfavorable for perovskite materials due to the existence of phase transition and the low decomposition temperature (around 85 °C).[15–20] Moreover, it is well-accepted that the stability of perovskites will be affected by light irradiation, humidity (aqueous vapor), and atmosphere (oxygen).[21–23] In order to obtain a stable device with high efficiency, significant research efforts have been devoted to optimize the property of perovskite materials, such as deposition techniques, composition regulating, as well as surface modification. For instance, using vapor-phase conversion growth method for improved crystal quality of the material; or doping different ions into A, B, and X sites[24] for relieved crystal stress or increased chemical bonds strength.[25] Nevertheless, these methods require atomic-level adjustment which is hard to control and will increase the cost of device production. Currently, most surface modification strategies for improving the stability of perovskite are simple external coating for isolation.[4,7,18,19] The surface passivation, such as molecular ligand passivation, requires great attention to the ratio of passivator and perovskite, and the type of passivator needs to be obtained through large numbers of experiments. These methods do have improved the

Dr. R. X. Li, Y. Q. Shi, X. Liu, Prof. R. Chen
Department of Electrical and Electronic Engineering
Southern University of Science and Technology
Shenzhen, Guangdong 518055, P. R. China
E-mail: chenr@sustech.edu.cn

Dr. R. X. Li, Dr. X. Fang, Dr. D. K. Wang, Prof. Z. P. Wei
State Key Laboratory of High Power Semiconductor Lasers
School of Science
Changchun University of Science and Technology
Changchun, Jilin 130022, P. R. China
E-mail: weizp@cust.edu.cn

Dr. R. X. Li
School of Electrical and Information Engineering
Guangxi University of Science and Technology
Liuzhou, Guangxi 545006, P. R. China

Dr. B. B. Li
College of New Materials and New Energies
Shenzhen Technology University
Shenzhen, Guangdong 518118, P. R. China

**ADVANCED
SCIENCE NEWS**

www.advancedsciencenews.com

**ADVANCED
MATERIALS**

www.advmat.de

stability of perovskite materials to a certain extent, but they are expensive and consumable. In addition, researchers gradually found that it is difficult to further improve the performance of perovskite devices, because of a large number of intrinsic defects created during growth. Based on various investigations more recently, since 2016, it is realized that defects have played a very important role in the stability of perovskite materials, and therefore, more attentions have been paid toward trap managements.[26–28]

The defects of perovskite materials discussed herein include shallow and deep level traps. It is needed to mention that most of the shallow level traps states (SLTS) come from point defects that do not affect the performance of material, according to the, namely, high defect tolerance property. The deep level traps states (DLTS) are often referred as "defects", and they are rarely studied. It is well-known that a series of defects have been created during the fabrication process of perovskite, and the defect density will gradually increase under environment of air, moisture, high temperature, and long-time light irradiation.[26,29] It will lead to nonradiative recombination and reduce the carrier migration rate, which affect the performance of the devices and even result in structural decomposition. Recent report by Stranks et al. has found that the DLTS are located at the grain boundaries, which shows the characteristics of hole trapping.[27] While Huang et al. have found that the DLTS are located at the surface dangling bonds, with density as large as 10^{17}–10^{18} cm^{-3}. In principle, the power conversion efficiency of perovskites solar cells can exceed 28.4% if reducing the density of DLTS.[28] Therefore, it is necessary to decrease the density of DLTS for improved material/device performance.

In this work, the organic–inorganic hybrid $CH_3NH_3PbBr_3$ (MAPbBr$_3$) perovskite microcrystal was encapsulated in a dense Al_2O_3 layer by atomic layer deposition (ALD) to form a micro-environment. It is interesting and surprising to find that this micron-level environment serves as a self-sufficient vacuum growth chamber, where the components of the perovskite are completely retained when sublimated, and the atoms will re-arrange after thermal treatment. The temperature-dependent X-ray powder diffraction (XRD) results indicated that the MAPbBr$_3$ microcrystals in the microenvironment maintain high crystal quality even at 250 °C. Using a home-made optical measurement system with tunable laser excitation and emission detection at different temperatures, the optical and lasing stability of the modified MAPbBr$_3$ has been characterized. It was found that the self-structural healing phenomenon takes place after annealing at 150 °C, and it showed 4.5-fold enhanced emission by reducing the DLTS density of nearly an order of magnitude. As a consequence, the modified MAPbBr$_3$ has shown stable emission and lasing for about 2 years. These results exhibited that high stability and high quality of perovskites can be achieved by decreasing DLTS, which also provide an important confidence for practical application of perovskites.

2. Results and Discussion

Typical energy band diagram of perovskite is shown in **Figure 1**a,[26] where the valence band maximum (VBM) is identified as the antibonding hybridization between Pb 6s and Br 4p

orbitals, and the conduction band minimum (CBM) is governed by the orbital interactions between Pb 6p and Br 4s orbitals in PbBr$_6$ octahedra.[30] The SLTS are close to the VBM and CBM, while the DLTS are more likely located in the middle between the two energy bands. As shown in Figure 1b, the SLTS generally come from point defects (interstitial, vacancy, interstitial impurity, etc.),[26] and in Figure 1c, the DLTS are always produced by grain boundaries and dangling bonds.[27,28] The size of MAPbBr$_3$ perovskite microcrystal used in this work is about 40 40 10 µm.[31] Figure 1d,e shows X-ray photoelectron spectroscopy (XPS) spectra of the binding energy of Pb 4f, Br 3d, O 1s, and Al 2p peaks of the as-grown and the encapsulated MAPbBr$_3$ perovskite (EMP), respectively. The Pb 4f spectra attributed to the PbBr$_6$ octahedra can be fitted with two pairs of spin–orbit split components of Pb 4f$_{5/2}$ and 4f$_{7/2}$ at 143 and 138.2 eV, and the Br 3d attributed to the CH$_3$Br can be fitted with Br 3d$_{3/2}$ and 3d$_{5/2}$ at 68.8 and 67.8 eV, respectively. The O 1s peak in the as-grown sample at 532.4 eV is attributed to the OH groups, which reduces after trimethylaluminium (TMA) pulses in the EMP sample. After the deposition of Al$_2$O$_3$ layer, the O 1s peak shows a new peak at 531.3 eV, which is attributed to Al−O. Besides, the Al 2p peak can be observed in the EMP sample that implying the Al$_2$O$_3$ has been successfully coated on the surface of perovskite.[32] Figure 1h–m shows the scanning electron microscopy (SEM) images and energy dispersive spectrometer (EDS) mapping of the EMP sample. Compared with the as-grown sample (shown in Figure S1, Supporting Information), the shape of the EMP sample is basically the same, indicating that this film has sufficient compactness and shape retention. Besides, it can be clearly seen that the EMP sample has relatively sharp edges, indicating that it is less affected by the surrounding environment. The EDS linear scanning of different thicknesses of the EMP samples also indicates that the Al$_2$O$_3$ has been successfully coated on the surface of perovskite, as shown in Figure S1 in the Supporting Information.

Temperature-dependent XRD measurements are performed and shown in **Figure 2**a. It can be seen that there are four distinct sharp peaks located at 14.7°, 29.9°, 45.7°, and 62.4°, which are assigned to the diffraction of (100), (200), (300), and (400) planes of MAPbBr$_3$ cubic crystal, respectively.[33] Note that the EMP sample has the same crystal orientation, implying the structure of the MAPbBr$_3$ microcrystal did not change during the growth of Al$_2$O$_3$. The related intensity ratio of the four main peaks of each sample (the as-grown sample and the ones coated by Al$_2$O$_3$ with different thickness of 100/300/500 nm, namely, EMP100, EMP300, EMP500, respectively) as a function of temperature is shown in Figure 2b. It can be seen that the intensity of four main diffraction peaks from all of the samples still maintain when the temperature increases to 180 °C. However, when the temperature is higher than 210 °C, the XRD diffraction peak of the as-grown and the EMP100 samples gradually disappears, while the other samples still exist even at 250 °C. This implies that encapsulation is beneficial for the improvement of perovskite structural and thermal stability. The thermogravimetric (TG) measurement also supports this claim which implies that the thicker the encapsulation, the slower the loss of the perovskite component (as shown in Figure S2, Supporting Information). Therefore, the EMP sample used below is the 500 nm thick encapsulated sample.
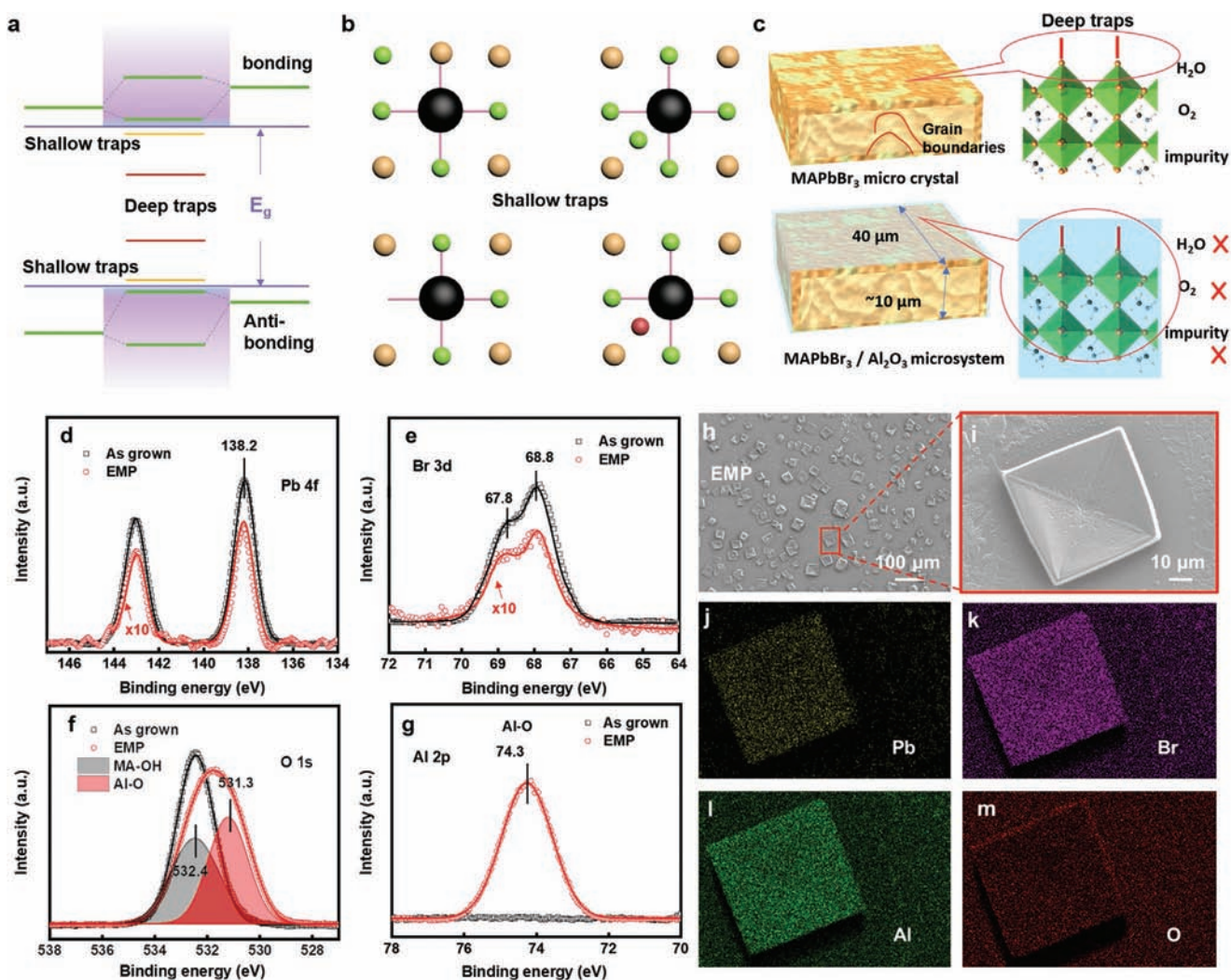
Figure 1. The schematic diagram of two types of traps and structural properties measurements. a) Typical energy band diagram of perovskite, and schematic diagram of the positions of the SLTS and the DLTS in the energy band. b,c) The types of the shallow and deep states trap in perovskite, and the schematic diagram of the as-grown sample and the EMP sample. The encapsulated sample can isolate water, oxygen, and impurities. d–g) XPS spectra of Pb 4f, Br 3d, O 1s, and Al 2p in the as-grown sample and the EMP sample. h,i) SEM image of the EMP sample and its enlarged picture. j–m) The corresponding EDS mapping images.

In order to analyze the optical properties of the as-grown and the EMP sample under different temperatures, temperature-dependent photoluminescence (PL) from room temperature (RT) to 100 °C was demonstrated. The schematic diagram of the optical measurement system is shown in **Figure 3**a, which is equipped with tunable laser excitation (325 and 442 nm) and emission detection at different temperatures. Figure 3b,c shows the PL spectra of the as-grown sample at 80 and 100 °C, respectively. It can be seen that the PL intensity recovers when the temperature of the sample cools down to RT from 80 °C, while it shows 40% decrease after annealing at 100 °C. Figure 3d,e shows the PL spectra of the EMP sample after annealing at 100 °C and the change of PL intensity over ten cycles. It can be seen that the PL intensity remains identical which implies that the thermal stability of the EMP sample is improved, and its structure is self-healed when returns to RT. It is because $MAPbBr_3$ material can easily release volatile gases CH_3NH_2

and HBr due to weak hydrogen bonding between MA and octahedral structure, which gives rise to the decreased PL intensity. However, when it is encapsulated, the gas cannot be released and the CH_3NH_2 and HBr will form $MAPbBr_3$ again when the sample is cooled down,[29] as shown in Figure 3f.

To further study the in-depth mechanism, a higher heat treatment of 150 °C (higher than its sublimation temperature) was used. This temperature was chosen because it is found that 150 °C is the optimal one for perovskite crystallization,[31] and the following discussions will mainly focus on this temperature. **Figure 4**a,b shows the corresponding temperature-dependent PL emission of the as-grown and the EMP sample, respectively. The left of the figures is the case from RT to 150 °C, and the right is from 150 °C to RT. In Figure 4a, it can be seen that the PL intensity decreases quickly with increased temperatures, and there is only 0.5% intensity left at 150 °C for the as-grown sample. Moreover, when the temperature cools down to RT, the PL intensity is

**ADVANCED
SCIENCE NEWS**

www.advancedsciencenews.com

**ADVANCED
MATERIALS**

www.advmat.de
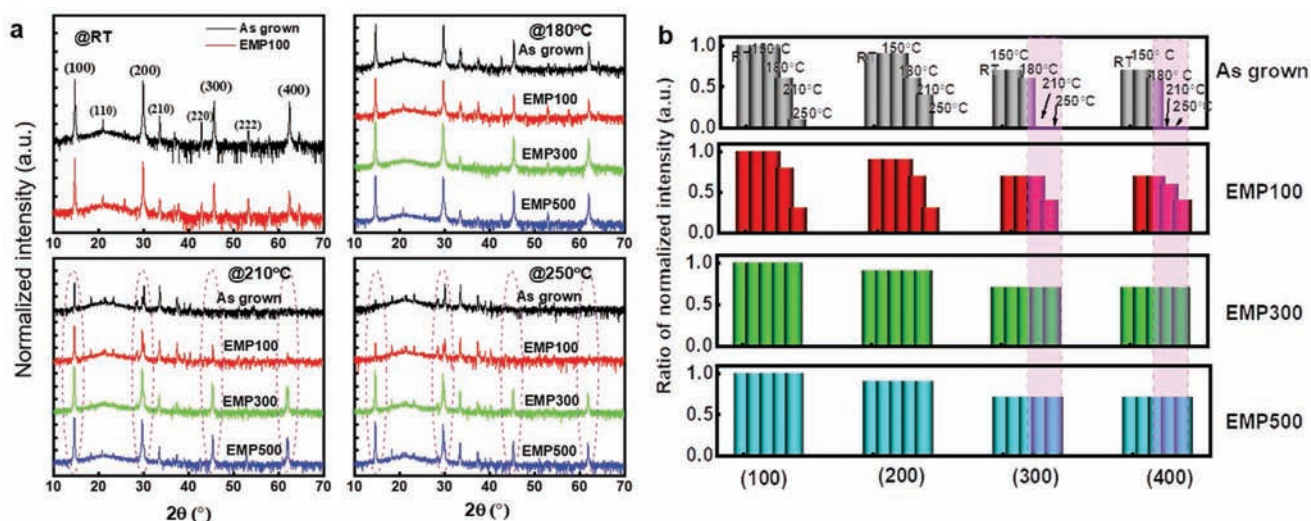
Figure 2. Thermal stability measurements. a) Variable temperature XRD diffraction patterns at RT to 250 °C. b) The intensity ratio of the four main patterns of each sample as a function of temperature.

unrecoverable, indicating that the as-grown sample is completely destroyed. The inset of Figure 4a shows the corresponding digital photos and the schematic diagram of the structure before and after treatment. It shows that there are many pits on the surface of the destroyed as-grown sample, especially at its four borders, which is consistent with the better thermal instability of the surface and borders. While in Figure 4b, it can be seen that the PL intensity decreases slowly with increased temperatures, and there is still 50% intensity left at 150 °C for the EMP sample. Moreover, it is interesting and surprising that when the temperature goes back to RT, the PL intensity shows 4.5 times enhancement (corresponding emission spectra are shown in Figure S3, Supporting Information). First, it shows that the encapsulated sample

has better thermal stability and optical properties. Second, different physical process should take place which is different from that for 100 °C. As can be seen in the schematic diagram shown in Figure 4d, there are many surface dangling bonds and bulk grain boundaries inside the EMP crystal before annealing. It can be verified by the corresponding digital photo shown below that there are many flaws on the crystal surface. They are brought about by crystal growth and will result in nonradiative recombination and DLTS emission (the peak position located at 690 nm, as shown in inset of Figure 4c). Moreover, these DLTS will cause structural instability, which will be described in detail below. While after annealing at 150 °C, the dangling bonds and grain boundaries are eliminated, and both of the crystal quality
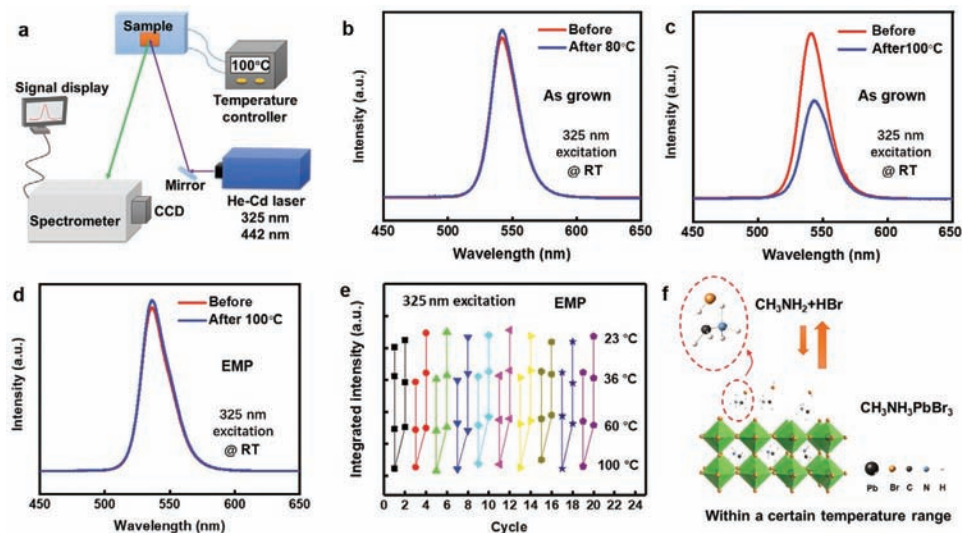
Figure 3. Optical stability measurements. a) Schematic diagram of the testing system, which includes a temperature controller, laser, and spectrometer. The laser has both 325 and 442 nm wavelengths, which are able to be switched in the same optical path. b,c) The PL spectra of the as-grown sample before and after annealing at 80 and 100 °C. d,e) The PL spectra of the EMP sample before and after annealing at 100 °C and its ten cycles of recovery of annealing. f) The schematic diagram of hydrogen bonds broken to generate recoverable gas CH_3NH_2 and HBr within a certain temperature range of thermal treatment, which cause intensity loss.
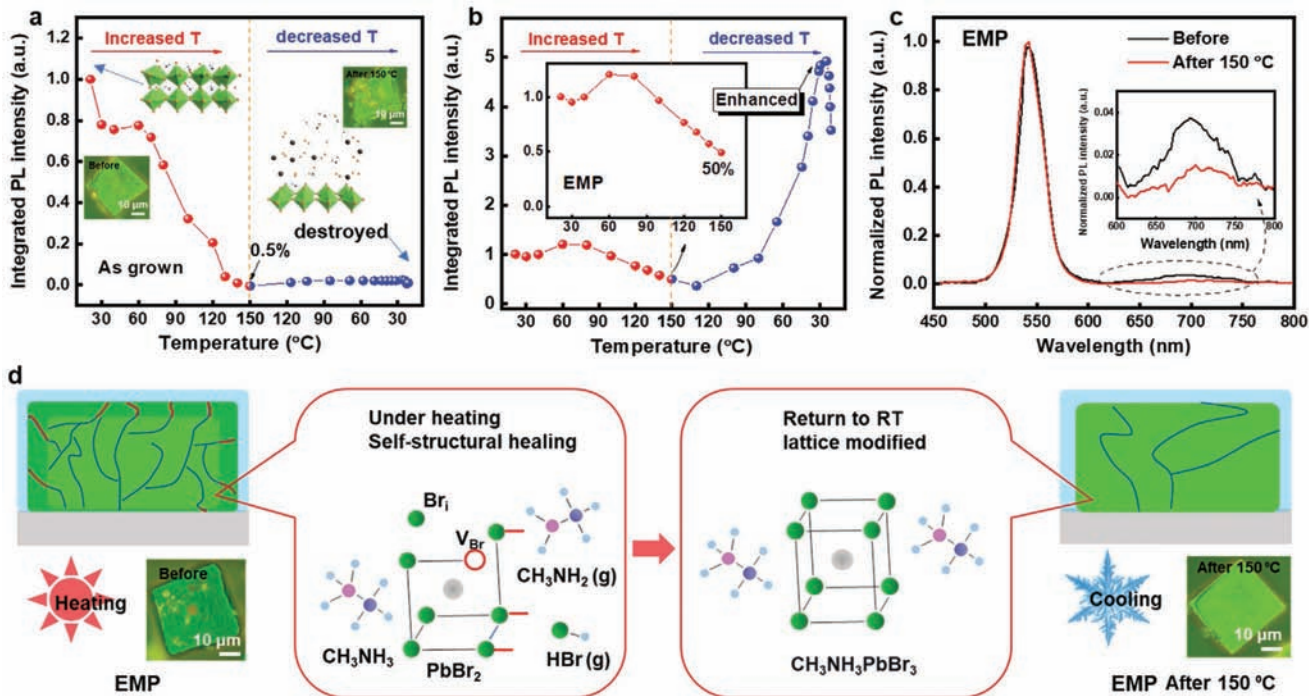
Figure 4. Mechanism of self-structural healing of the EMP sample. a,b) The relationship of PL integrated intensity and temperature of the as-grown sample and the EMP sample from RT to 150 °C, then back to RT. c) The normalized PL spectra of the EMP sample after annealing at 150 °C. d) Schematic diagram of the self-structural regrowth of MAPbBr$_3$ perovskite microenvironment for optical improvement after annealing at 150 °C.

and optical properties are improved, as shown in the right of Figure 4d. From the corresponding digital image, it can be clearly seen that the surface of the modified EMP sample is flattened, and there are no obvious flaws on it. Therefore, this micron-level environment provides a high-vacuum growth like chamber, where the components of the perovskite (CH$_3$NH$_2$ and HBr) are completely retained when sublimated. The crystal structure will be re-grown under the action of stress and the gravitational effect

of hydrogen bonds (CH$_3$NH$_2$ HBr MAPbBr$_3$), which results in the elimination of DLTS when it cools down to RT. A schematic diagram of this process is shown in the inset of Figure 4d. Therefore, the PL intensity increased by 4.5 times, and the DLTS emission decreased as shown in the inset of Figure 4c and Figure S3 in the Supporting Information.

Figure 5a,b shows the different effects on the optical properties of the as-grown and the EMP samples under
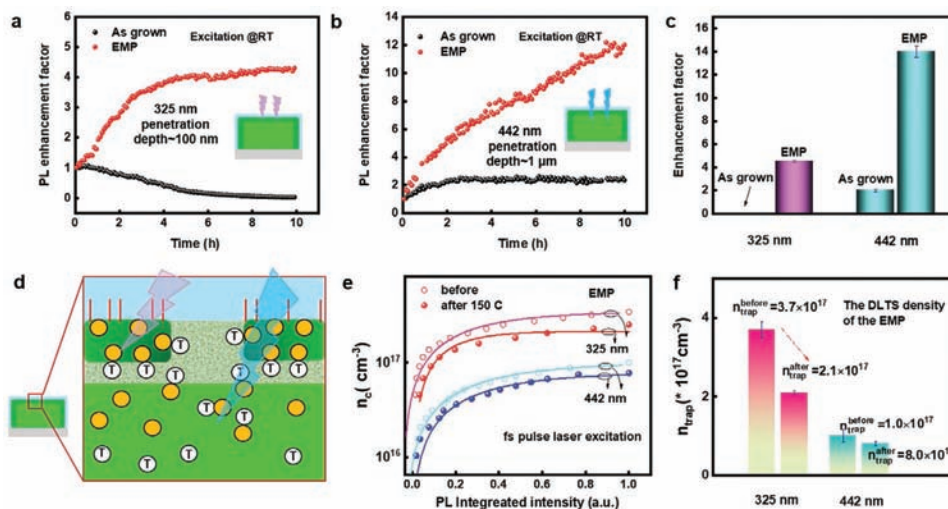
Figure 5. The evolution of the DLTS. a,b) Long-time photostability tests up to 10 h illumination by 325 and 442 nm of samples. c) Enhancement factors after 10 h illumination of (a) and (b). d) The mechanism of attenuation and enhancement caused by laser irradiation. e) The evolution of the DLTS at the surface and bulk of the material as a function of photogenerated carrier density. f) Corresponding changes in the value of the DLTS density.

**ADVANCED
SCIENCE NEWS**

www.advancedsciencenews.com

**ADVANCED
MATERIALS**

www.advmat.de

long-time irradiation (10 h) of 325 and 442 nm continuous wave (CW) laser, respectively. The black and the red dotted lines represent the PL intensity of the as-grown and the EMP samples, respectively. It can be seen in Figure 5a that compared with the completely destroyed as-grown sample, the EMP sample shows a 4.5-fold enhancement under the 325 nm laser irradiation. While in Figure 5b, both of the PL intensity of the as-grown and the EMP sample are enhanced, and have about two times for the as-grown sample and 14 times for the EMP sample under the 442 nm laser irradiation (the values are shown in Figure 5c). It is demonstrated that compared with 442 nm laser, 325 nm laser is more destructive to perovskite. It is because the penetration depth of the 325 nm laser is smaller than 442 nm, and the excited area of the 325 nm laser is near the surface-dangling-bonds region. In addition, it may be related to the photon energy. The band gap of MAPbBr$_3$ is 2.29 eV, when the samples are excited at 325 (3.8 eV) and 442 nm (2.8 eV), it will have 1.51 and 0.51 eV of energy higher than the band gap, respectively. It is noted that the 1.51 eV is higher than the thermal energy of breaking N−H bonds (1.4 eV). This implies that the extra energy can convert into thermal energy through electron–phonon interaction, which results in a similar effect with the thermal treatment. Thus, the surface dangling bonds are easier to be interrupted, and then the structure of perovskite will decompose from surface to bulk (the black dotted line in Figure 5a).[28] However, the EMP sample possesses a self-sufficient vacuum growth chamber, where a dynamic process of bonds broken and re-grown takes place for enhanced PL intensity (the red dotted line in Figure 5a). While for the 442 nm laser, which has a larger penetration depth and the excited area is closer to the grain boundary in the bulk. The grain boundary has hole-trapping characteristics that are able to trap migrating ions to eliminate the DLTS, as shown in Figure 5d.[28] Thus, it results in two times enhancement of the as-grown and 14 times enhancement in the EMP sample. Therefore, the evolution of the DLTS density at the surface and bulk can be analyzed by different penetration depths, as shown in Figure 5e,f, which is a function of photogenerated carrier density.

In order to obtain the evolution of the DLTS density in this process, 325 and 442 nm femtosecond laser pulses were used for measurement due to the negligible trap states depopulation during the luminescent period.[2] Under low fluence femtosecond laser excitation, the dynamics of photogenerated charge carrier density $n_c(t)$ can be described by the following equations[34,35]

$$\frac{dn_c(t)}{dt} = -\sum_i a_i n_c(t) n_{tp}^i(t) - \frac{n_c(t)}{\tau_0} \tag{1}$$

$$\frac{dn_{tp}^i(t)}{dt} = -a_i n_c(t) n_{tp}^i(t) \tag{2}$$

where $n_{tp}^i(t)$ is the trap states density and a_i is the capture coefficient, representing the ability of the trap centers to capture carriers, and τ_0 is the lifetime of carriers under low fluence. Therefore, the first term in Equation (1) represents trap-mediated nonradiative pathways, and the second term represents the radiative recombination. From the relationship between the integrated band edge PL intensity ($I_{PL} = k \int_0^\infty n_c(t)/\tau_0 dt$, where k is

a constant), the initial photogenerated charge carrier density $n_c(0)$ can be obtained as

$$n_c(0) = \sum_i n_{tp}^i(0)\left(1 - e^{-a_i \tau_0 I_{PL}/k}\right) + I_{PL}/k \tag{3}$$

Considering the surface region was photoexcited by 325 nm laser while the bulk region was excited by 442 nm laser, fitting the experimental result with Equation (3) will enable us to obtain the changes of the DLTS density before and after annealing at 150 °C. The result is shown in Figure 5e, and the values are shown in Figure 5f. Therefore, the DLTS density, namely, the surface dangling bonds and the bulk grain boundary, is 3.7×10^{17} cm^{-3} and 2.1×10^{17} cm^{-3} for the EMP sample before annealing, and they become 1.0×10^{17} and 8.0×10^{16} cm^{-3} after annealing, respectively. It shows that both of the DLTS density from the surface and bulk decreased after annealing at 150 °C, especially the surface DLTS density, which decreases nearly an order of magnitude.

To verify this claim, the emission and lasing stability were performed. Figure S4a,b in the Supporting Information shows that the lasing threshold of the as-grown and the modified EMP sample is about 9 μJ cm^{-2} determined from the collected μ-PL spectrum under different excitation densities from a single microcrystal at RT. **Figure 6**a,b shows the lasing intensity of the as-grown and EMP sample as a function of time under an excitation intensity of 15 μJ cm^{-2}. It can be clearly seen that the lasing intensity of the as-grown sample rapidly decreases in the first 60 min, while the modified EMP sample still remains at 95% after 400 min, as shown in Figure 6c. Moreover, the optical stability of the as-grown and the EMP sample before and after annealing at 150 °C has been promoted and shown in Figure 6d. It can be seen that the as-grown sample only has about 15% intensity after about 2 years at RT, while the EMP samples before and after annealing still have good emission characteristics, especially for the modified one. In addition, after about 2 years, the lasing stability of the modified EMP sample still remains the same, as shown in Figure S5 in the Supporting Information. Therefore, after the reduction of DLTS density, the optical and lasing stability of the samples have been greatly improved.

3. Conclusion

In summary, a self-sufficient micron-level vacuum growth chamber was proposed for perovskite material in this work. The MAPbBr$_3$ microcrystals were encapsulated in a very dense Al$_2$O$_3$ layer by ALD. In this micron-level chamber, the MAPbBr$_3$ microcrystals are able to effectively prevent water and oxygen, and the thermal and optical stability of them has been greatly improved. It was found that the EMP sample is able to maintain high crystal quality at 250 °C. Moreover, the crystal structure will be re-grown rather than "lattice adjustment" under the action of stress and the gravitational effect of hydrogen bonds after annealing at 150 °C (higher than its sublimation temperature). It is because the components of the perovskite are completely retained when sublimated, and during the re-growth process, the DLTS decrease nearly an order of magnitude, which are recognized as the key issue that results
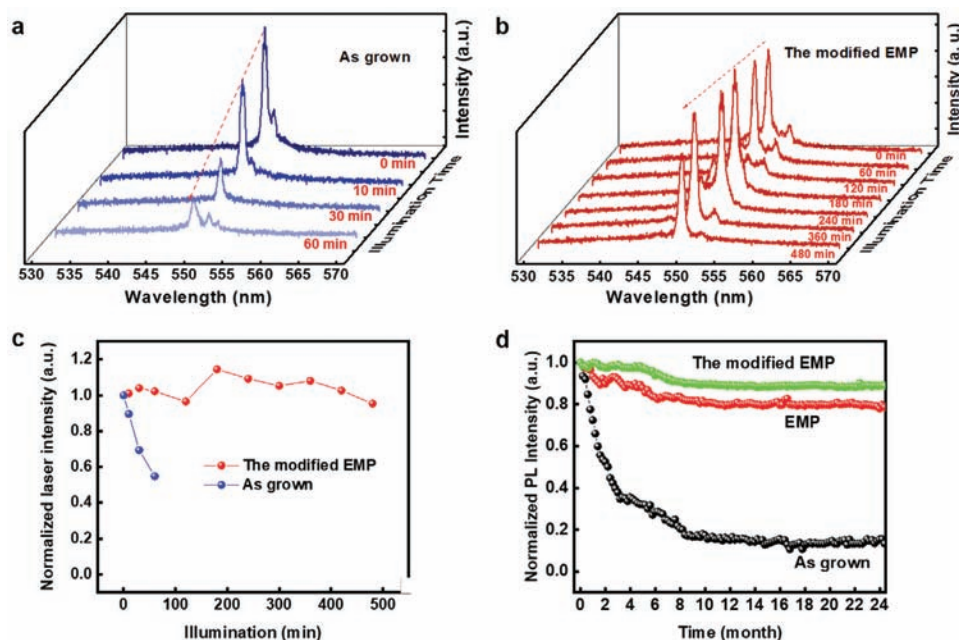
Figure 6. The optical and lasing stability measurements. a,b) The lasing intensity of the as-grown sample and the modified EMP sample as a function of time under an excitation intensity of 15 μJ cm^{-2}. c) The corresponding intensity trend. d) Optical stability test of the as-grown and the EMP sample before and after annealing at 150 °C in 2 years.

in the improvement of device performance. Therefore, the PL intensity enhanced 4–14 times, while the emission and lasing stability was maintained up to 2 years. This research work has provided an effective route and experimental references to achieve perovskites with good stability and high quality, which would be useful for perovskite materials and devices.

4. Experimental Section

Materials: CH$_3$NH$_3$Br, PbBr$_2$ (99.99%, Xi'an Polymer Light Technology), and dimethyl formamide solvent (DMF, J&K Scientific) were used. All salts and solvents were used as received without any further purification.

Synthesis of MAPbBr$_3$ Perovskite Microcrystals: The perovskite microcrystals were synthesized by one-step solution deposition. A more detailed description of the growth process can be found in ref [18]. 0.112 g of CH$_3$NH$_3$Br and 0.367 g of PbBr$_2$ were mixed in dimethyl formamide solvent to form precursor solution. Then stirred overnight under 60 °C. A pipette was used to measure 5 μL perovskite solution to drop onto 2 cm × 6 cm glass substrate and spread out uniformly. Note that all the substrates were cleaned and treated with oxygen-plasma to improve the surface hydrophilicity before being used. Finally, the samples were annealed under 90 °C for about 10 min to generate microcrystals.[31]

Synthesis of MAPbBr$_3$-Al$_2$O$_3$ Micro-Matrix Composites: The prepared microcrystals were placed into the growth chamber of ALD system (LabNano PE ALD system from Bei Jing Ensure Nanotech). Oxygen plasma and TMA were selected as raw materials for the synthesis of Al$_2$O$_3$ films, providing pulse precursor of "oxygen" element and "Al" element, respectively. High purity Ar (99.9%) was used as a purging and carrier gas, and its flow was controlled by mass flow controller (MFC, 15 sccm for purging). The oxygen flow was 10 sccm, which was also controlled by MFC. A typical PEALD Al$_2$O$_3$ growth cycle was composed of 25 ms of TMA exposure, 5 sccm of Ar purging, 10 sccm of oxygen plasma exposure with RF power of 200 W for 6 s. The waiting time was 30 and 15 s, respectively. The deposition temperature was room temperature. In this deposition process, growth rate was 2.1 Å per cycle.

Thus, the total growth cycles were 480, 1430, and 2381 for A100, A300, and A500 sample, respectively.

Structure Characterization: The surface chemical property of the MAPbBr$_3$ microcrystals and MAPbBr$_3$-Al$_2$O$_3$ micro-matrix composites samples was analyzed by XPS (Thermo Fisher Scientific, 250Xi) by using Al Ka radiation source (excitation energy of 1486.6 eV). The crystal structure of the samples under the range of RT to 250 °C was characterized by XRD on a Rigaku TTR3 X-ray Diffraction System. The field-emission SEM (ZEISS Gemini SEM 300) equipped with EDS was used to measure the microstructures and elemental analysis of the samples. The TG analysis (TA Q500) was carried out under nitrogen flow from RT to 800 °C.

Optical Characterizations: Steady-state PL spectra were measured by a Shamrock spectrometer (model no. SR-750-D1-R) and detected by a Newton CCD (model no. DU920P-BU). A He-Cd CW laser with line of 325 and 442 nm as the excitation source was used to perform PL and long-time irradiation measurements. The power of the excitation laser was 1 mW, and the spot size was around 0.03 cm^2. The 325 and 442 nm femtosecond pulses were selected (Coherent Astrella ultrafast Ti:sapphire laser with OperA Solo, pulse with of 100 fs and repetition rate of 1 kHz) to perform the power-dependent PL measurement for the evolution of the DLTS density. The temperature was maintained at RT–150 °C for in situ steady-state PL. The long-term photostability tests under 325 and 442 nm excitation were obtained by time-correlated Hamamatsu H7422-02 photomultiplier tube. For the lasing characterization, the 450 nm femtosecond pulsed laser was used as the excitation source. The pumping laser was focused via a ×40 objective and the laser spot diameter was controlled by manipulating the collimation of the pumping beam. According to the grating of 600 g mm^{-1}, 26 μm pixel size of the camera, and 100 μm of slit width, the spectral resolution of the optical measurement was determined to be around 0.24 nm.

Supporting Information

Supporting Information is available from the Wiley Online Library or from the author.

**ADVANCED
SCIENCE NEWS**

www.advancedsciencenews.com

**ADVANCED
MATERIALS**

www.advmat.de

Acknowledgements

Conﬂict of Interest

The authors declare no conﬂict of interest.

Data Availability Statement

Research data are not shared.

Keywords

[1] Q. Dong, Y. Fang, Y. Shao, P. Mulligan, J. Qiu, L. Cao, J. Huang, *Science* **2015**, *347*, 967.

[2] E. T. Hoke, D. J. Slotcavage, E. R. Dohner, A. R. Bowring, H. I. Karunadasa, M. D. McGehee, *Chem. Sci.* **2015**, *6*, 613.

[3] S. Wang, J. Yu, M. Zhang, D. Chen, C. Li, R. Chen, G. Jia, A. L. Rogach, X. Yang, *Nano Lett.* **2019**, *19*, 6315.

[4] R. Li, J. Yu, S. Wang, Y. Shi, Z. Wang, K. Wang, Z. Ni, X. Yang, Z. Wei, R. Chen, *Nanoscale* **2020**, *12*, 13360.

[5] N. Zibouche, M. S. Islam, *ACS Appl. Mater. Interfaces* **2020**, *12*, 15328.

[6] A. Perulli, A. Balena, M. Fernandez, G. Nedelcu, A. Cretí, M. V. Kovalenko, M. Lomascolo, M. Anni, *Appl. Phys. Lett.* **2018**, *112*, 171904.

[7] Q. Jiang, Y. Zhao, X. Zhang, X. Yang, Y. Chen, Z. Chu, Q. Ye, X. Li, Z. Yin, J. You, *Nat. Photonics* **2019**, *13*, 460.

[8] Nrel National Center for Photovoltaics Best Research-Cell Efﬁciency Chart, https://www.nrel.gov/pv/cell-efﬁciency.html (accessed: October 2020).

[9] Y. Fu, H. Zhu, J. Chen, M. P. Hautzinger, X. Y. Zhu, S. Jin, *Rev. Mater.* **2019**, *4*, 169.

[10] H. Baker, D. Strandell, P. Kambhampati, *J. Phys. Chem. C* **2020**, *124*, 18816.

[11] E. P. Booker, T. H. Thomas, C. Quarti, M. R. Stanton, C. D. Dashwood, A. J. Gillett, J. M. Richter, A. J. Pearson, N. J. L. K. Davis, H. Sirringhaus, M. B. Price, N. C. Greenham, D. Beljonne, S. E. Dutton, F. Deschler, *J. Am. Chem. Soc.* **2017**, *139*, 18632.

[12] H. Sun, W. Tian, X. Wang, K. Deng, J. Xiong, L. Li, *Adv. Mater.* **2020**, *32*, 1908108.

[13] S. A. Bourelle, R. Shivanna, F. V. A. Camargo, S. Ghosh, A. J. Gillett, S. P. Senanayak, S. Feldmann, L. Eyre, A. Ashoka, T. W. J. van de Goor, H. Abolins, T. Winkler, G. Cerullo, R. H. Friend, F. Deschler, *Nano Lett.* **2020**, *20*, 5678.

[14] H. Seiler, S. Palato, C. Sonnichsen, H. Baker, E. Socie, D. P. Strandell, P. Kambhampati, *Nat. Commun.* **2019**, *10*, 4962.

[15] A. J. Knight, A. D. Wright, J. B. Patel, D. P. McMeekin, H. J. Snaith, M. B. Johnston, L. M. Herz, *ACS Energy Lett.* **2019**, *4*, 75.

[16] T. W. Jones, A. Osherov, M. Alsari, M. Sponseller, B. C. Duck, Y. K. Jung, C. Settens, F. Niroui, R. Brenes, C. V. Stan, Y. Li, M. Abdi Jalebi, N. Tamura, J. E. Macdonald, M. Burghammer, R. H. Friend, V. Bulovi, A. Walsh, G. J. Wilson, S. Lilliu, S. D. Stranks, *Energy Environ. Sci.* **2019**, *12*, 596.

[17] J. Zhao, Y. Deng, H. Wei, X. Zheng, Z. Yu, Y. Shao, J. E. Shield, J. Huang, *Sci. Adv.* **2017**, *3*, eaao5616.

[18] L. Liu, L. Deng, S. Huang, P. Zhang, J. Linnros, H. Zhong, I. Sychugov, *J. Phys. Chem. Lett.* **2019**, *10*, 864.

[19] I. Deretzis, E. Smecca, G. Mannino, A. La Magna, T. Miyasaka, A. Alberti, *J. Phys. Chem. Lett.* **2018**, *9*, 3000.

[20] B. Conings, J. Drijkoningen, N. Gauquelin, A. Babayigit, J. D'Haen, L. D'Olieslaeger, A. Ethirajan, J. Verbeeck, J. Manca, E. Mosconi, F. D. Angelis, H. G. Boyen, *Adv. Energy Mater.* **2015**, *5*, 1500477.

[21] A. Aziz, N. Aristidou, X. Bu, R. J. E. Westbrook, S. A. Haque, M. S. Islam, *Chem. Mater.* **2020**, *32*, 400.

[22] M. L. De Giorgi, T. Lippolis, N. F. Jamaludin, C. Soci, A. Bruno, M. Anni, *J. Phys. Chem. C* **2020**, *124*, 10696.

[23] M. Anni, A. Cretì, Y. Zhang, M. L. De Giorgi, M. Lomascolo, *Appl. Sci.* **2020**, *10*, 2148.

[24] R. Li, S. Chen, X. Li, G. Yin, Y. Gong, J. Yu, G. Pang, J. Liu, Y. Liu, Z. Ni, L. Zhang, R. Chen, H. L. Wang, *Nanoscale* **2020**, *12*, 3692.

[25] Q. Liao, X. Jin, H. Fu, *Adv. Opt. Mater.* **2019**, *7*, 1900099.

[26] H. Jin, E. Debroye, M. Keshavarz, I. G. Scheblykin, M. B. J. Roefﬂaers, J. Hofkens, J. A. Steele, *Mater. Horiz.* **2020**, *7*, 397.

[27] T. A. S. Doherty, A. J. Winchester, S. Macpherson, D. N. Johnstone, V. Pareek, E. M. Tennyson, S. Kosar, F. U. Kosasih, M. Anaya, M. Abdi Jalebi, Z. Andaji Garmaroudi, E. L. Wong, J. Madéo, Y. H. Chiang, J. S. Park, Y. K. Jung, C. E. Petoukhof, G. Divitini, M. K. L. Man, C. Ducati, A. Walsh, P. A. Midgley, K. M. Dani, S. D. Stranks, *Nature* **2020**, *580*, 360.

[28] Z. Ni, C. Bao, Y. Liu, Q. Jiang, W. Q. Wu, S. Chen, X. Dai, B. Chen, B. Hartweg, Z. Yu, Z. Holman, J. Huang, *Science* **2020**, *367*, 1352.

[29] E. J. Juarez-Perez, L. K. Ono, M. Maeda, Y. Jiang, Z. Hawash, Y. Qi, *J. Mater. Chem. A* **2018**, *6*, 9604.

[30] G. Xiao, Y. Cao, G. Qi, L. Wang, C. Liu, Z. Ma, X. Yang, Y. Sui, W. Zheng, B. Zou, *J. Am. Chem. Soc.* **2017**, *139*, 10087.

[31] B. Li, T. Zhou, X. Fang, W. Zhang, X. Li, Z. Guan, J. Li, L. Wang, S. Hark, Z. Zhang, *J. Mater. Chem. C* **2019**, *7*, 4102.

[32] M. Kot, L. Kegelmann, C. Das, P. Kus, N. Tsud, I. Matolinova, S. Albrecht, V. Matolin, D. Schmeisser, *ChemSusChem* **2018**, *11*, 3640.

[33] J. Ding, Y. Zhao, S. Du, Y. Sun, H. Cui, X. Zhan, X. Cheng, L. Jing, *J. Mater. Sci.* **2017**, *52*, 7907.

[34] G. Xing, N. Mathews, S. S. Lim, N. Yantara, X. Liu, D. Sabba, M. Grätzel, S. Mhaisalkar, T. C. Sum, *Nat. Mater.* **2014**, *13*, 476.

[35] Y. Ren, W. Wang, Z. Wang, S. Xia, Y. Wang, *J. Phys. Chem. C* **2020**, *124*, 8341.